3D PRINTED MULTIMATERIAL MICROFLUIDIC TRANSISTORS

Alireza Ahmadianyazdi[¥,1], Wei Huang[¥,1,2], Kaustav A. Gopinathan[¥,3], Ivan Stepanov[*,1,4], Lisa Horowitz[1], Ting-Yuan Tu[2], Mehmet Toner[3,5], and Albert Folch[1]

[1]Department of Bioengineering, University of Washington, Seattle, WA, 98195

[2] Department of Biomedical Engineering, College of Engineering, National Cheng Kung University, Tainan 70101, Taiwan (R.O.C)

[3]Center for Engineering in Medicine & Surgery, and Department of Surgery Massachusetts General Hospital, Boston, MA 02114

[4]Department of Mechanical Engineering, University of Washington, Seattle, WA, 98195

[5]Shriners Children's, Boston, MA 02114

[*]Corresponding author, e-mail address: steiva@uw.edu

[¥]These three authors contributed equally to this work.

Abstract

Microfluidic actuators, including elastomeric microvalves and microfluidic transistors, are increasingly used to augment and simplify flow automation. The vast majority of these actuators regulate flow using microfabricated, thin membranes that are inherently difficult to fabricate and integrate into small devices. The performance of these actuator platforms is critically determined by the membrane's mechanical performance, which calls for scalable and reliable membrane microfabrication techniques. Previous approaches for manufacturing elastomeric membranes in microfluidic actuators enabled either their high-resolution fabrication (*e.g.*, soft lithography) or their facile manufacturability (*e.g.*, 3D printing), but not both. Here we present a photopolymer resin that closely mimics the Young's Modulus (elasticity) and reversible stretchability (no hysteresis) of poly(dimethylsiloxane) (PDMS) without compromising its high resolution or biocompatibility. This development enables the fabrication of microfluidic transistors (*i.e.,* microvalves capable of proportional amplification) by multimaterial stereolithography (mSLA). Our mSLA-printed microfluidic transistors display proportional pressure amplification occasionally reaching large intrinsic gains (>300), although reliably printing complex multi-transistor devices will require high-resolution 3D-printers. Moreover, the absence of hysteresis overcomes a longstanding problem of unequal opening and closing thresholds found in most microfluidic actuators, allowing us to demonstrate the first mSLA-printed pressure amplifiers. This work represents an advancement towards building more complex microfluidic automats.

Keyword: Microfluidics, 3D-printing, Stereolithography, PDMS, Automation

1. Introduction

Microfluidic actuators have become an indispensable technology in fields such as genomics,[1,2] proteomics,[3,4] pharmaceutical testing,[5,6] cell biology,[7] tissue engineering,[8] polymer synthesis,[9] micromixers,[10] and organs-on-chips,[6,11] to cite a few. Since the advent of the first elastomeric microfluidic valves made in poly(dimethylsiloxane) (PDMS),[12] most microfluidic actuators have relied on a flexible membrane to modulate fluid flow.[13] Unfortunately, the manufacturing challenges of soft lithography techniques, including high costs, scalability limitations, labor-intensive processes, and the need for specialized expertise, hinder the large-scale adoption of fluid automation technology among microfluidic engineers.[14] Additionally, the 2D-layered nature of soft lithography makes highly interconnected and component-dense microfluidic chips challenging to fabricate, as PDMS interconnects remain difficult to route without 3D fabrication capabilities.[15]

3D printing can address the limitations encountered in the manufacturing of microfluidic actuators.[16–19] Sochol *et al*. multijet-printed microfluidic components such as fluidic capacitors, diodes, and valves.[20] A recent 3D nanoprinted normally closed microfluidic transistor[21] achieved high resolution by direct laser writing (DLW), although the narrow material choice and small patterning capability of DLW made optimization and connectorization (modularity) difficult. At the other end of the size spectrum, the relatively flexible constraints in robotics have seen a flourishing of soft multifunctional materials[22–25] and of 3D printed fluidic actuators and controllers for soft robots.[26–33] However, these actuators with bending features typically on the centimeter scale are not suitable for microfluidic applications. Synergies between soft robotics and microfluidics have been anticipated,[34–36] but 3D printing of soft microrobots is still an emerging field.[37] As the complexity of microfluidic chips continues to grow, next generation technologies capable of high-resolution multimaterial fabrication will be essential to handle the intricate routing and component density of these circuits.

Towards that goal, here we demonstrate the use of multimaterial stereolithography (mSLA)[38–40] to 3D print a microfluidic transistor,[41] a type of microfluidic actuator whose key capability to proportionally amplify fluidic signals is critically influenced by the membrane material. We demonstrated devices made of transistors such as pressure amplifiers that require that the membranes be printed with a material of very low Young's modulus and negligible hysteresis (like PDMS). Since PDMS and other elastomers are challenging to 3D print at high resolution without using absorbers,[42,43] we developed novel acrylate-based SLA resins that yield high resolution and

feature mechanical properties similar to PDMS. SLA has long served as a tool to build high-resolution microfluidic devices and valves in 3D architectures,[17–19,44–47] overcoming the manufacturing obstacles of soft lithography. We used a "print-pause-print" mSLA process to build multimaterial hybrid structures.[48,49] (It is important to note that the terminology "print-pause-print" has also been used to refer to an alternative strategy for embedding dissimilar-material objects in the print.[50])

2. Results

2.a. The difference between a microvalve and a microfluidic transistor: How flow limitation arises

A microfluidic transistor is a microvalve that can proportionally amplify a fluidic signal.[41] Transistors, both electronic and microfluidic, achieve high gain amplification through a crucial non-linear behavior of self-regulation of the output signal (which is current in electronics and flow in microfluidics). Transistors show self-regulation when they are operated under specific conditions. Specifically, this self-regulatory behavior is what gives the transistor its high output impedance, and therefore a high (>1) intrinsic gain.[51] In electronic field-effect transistors (FETs), the self-regulatory behavior is known as "saturation". In microfluidic transistors, the behavior is known as "flow limitation."[41]

First-order analysis of the valve helps understand why the transistor behavior arises. Like an FET (**Fig. 1**A), a microfluidic transistor (**Fig. 1**B) consists of three terminals, namely the source, the drain, and the gate. The gate is built as a valve. (Note that not every valve works well as a gate.) Similar to the controlling of drain current I_D in FETs via the externally applied gate-to-source voltage V_{GS} (a condition called "reverse bias"), the drain flow rate Q_D in microfluidic transistors can be controlled by the externally applied gate-to-source pressure P_{GS}. By analogy to FETs, microfluidic transistors should show self-regulation when P_{GS} = ct., *i.e.,* the gate pressure is adjusted at the same rate as the source pressure, to maintain the "reverse bias" condition that is typical of FETs. In addition, the transistor is designed such that the resistance of the gate region R_G is larger than that of the rest of the channel R_{ch} even when the valve is at rest. In our case, the main channel is 6.2 mm long (from inlet to outlet, not counting the valve), 800 μm wide, and 180 μm high, whereas the valve is 0.8 mm long, 800 μm wide, and 80 μm high. Using the approximate expression of flow resistance R for a rectangular channel,

$$R \approx \frac{12\eta L}{\omega h^3 (1 - 0.63\, h/\omega)} \qquad \text{(Eqn. 1)}$$

where η is the viscosity and L, h and w are the length, height, and width of the channel, respectively, we obtain that R_G ~ 1.35 R_{ch} when the valve is at rest.

Self-regulation is achieved in our devices because, by keeping P_{GS} = ct., any increases in absolute P_S (which increase Q_D) are operationally matched by increases in absolute P_G (which decrease Q_D by gradually closing the valve). **Fig. 1**C&D conceptually illustrates the behavior of an example microfluidic transistor when P_S is increased from 1 to 10 (a.u.) while maintaining P_{GS} = 0 and the drain at atmosphere (P_D = 0). For simplicity, here the device is assumed to be symmetric and the valve small, so the pressure inside the channel at the valve seat is approximately P_M = (P_D + P_S)/2 = P_S / 2. **Fig. 1**C schematically shows how, to maintain P_{GS} = 0, the application of a small P_S = 1 also constrains P_G = 1, resulting in an even smaller transmembrane pressure of P_G - P_M = 0.5 that bends the membrane slightly. On the other hand, when the application of a large P_S = 10 (a.u.) constrains P_G = 10 (**Fig. 1**D) to maintain P_{GS} = 0, the transmembrane pressure P_G - P_M = 5 bends the membrane significantly.

We are interested in evaluating the flow rate at the drain as a function of P_{SD}, $Q_D = P_{SD}/(R_{Ch}+R_G)$, with R_{ch} ~ 0.743 R_G (for our transistor) and $R_G = f(P_{SD})$. For our transistor, it can be shown that, given the expression

$$K \equiv \frac{L^4}{60Et^3} \quad \text{(Eqn. 2)}$$

where L is the length of the channel, t is the membrane thickness, and E is the Young's Modulus of the membrane material, then the function $Q_D(P_{SD})$ can be approximated as (see section S1 in Suppl. Info. for derivation):

$$Q_D(P_{SD}) = \frac{P_{SD}}{R_{Ch}+R_G} = \frac{\omega H^3}{12\eta L} \; \frac{P_{SD}}{0.743 + \frac{1}{\left(1 - \frac{L^4}{60EHt^3}\left[P_{GS} + \frac{P_{SD}}{2}\right]\right)^3}} \quad \text{(Eqn. 3)}$$

Eqn. 3 helps explain why experimentally flow limitation is found to be so sensitive to variations in L and t, requiring in the future high-precision manufacturing techniques. We can use graphing software to simulate the function $Q_D(P_{SD})$ for various cases. In the purely elastic case, the Young's Modulus E is independent of P_{SD} and the function $Q_D(P_{SD})$ has a shape that is clearly linear for small P_{SD} but decays (unrealistically) for large P_{SD} (**Fig. 1**E). On the other hand, for a $E(P_{SD})$ function that increases linearly by ~40% of the initial (elastic-case) value as pressure increases from 0 to 15 psi (a more realistic assumption, as the stiffness of most elastic materials increases with

deformation), we obtain a more experimentally-realistic “flattening shape” at large P_{SD} (characteristic of flow limitation) while maintaining the same linear slope at small P_{SD} (**Fig. 1**F). More complex $E(P_{SD})$ functions are possible. This Q_D vs P_{SD} behavior for large P_{SD}, equivalent to the I_D vs V_{SD} behavior called *saturation* in electronic FETs (**Fig. 1**G), is called *flow limitation* in microfluidics (as recently reported in PDMS valves by Gopinathan *et al*.[41]). We conclude that the non-linear elastic deformation behavior of the membrane at large P_{SD} provides a satisfactory first-order explanation for the appearance of flow limitation in microfluidic transistors.

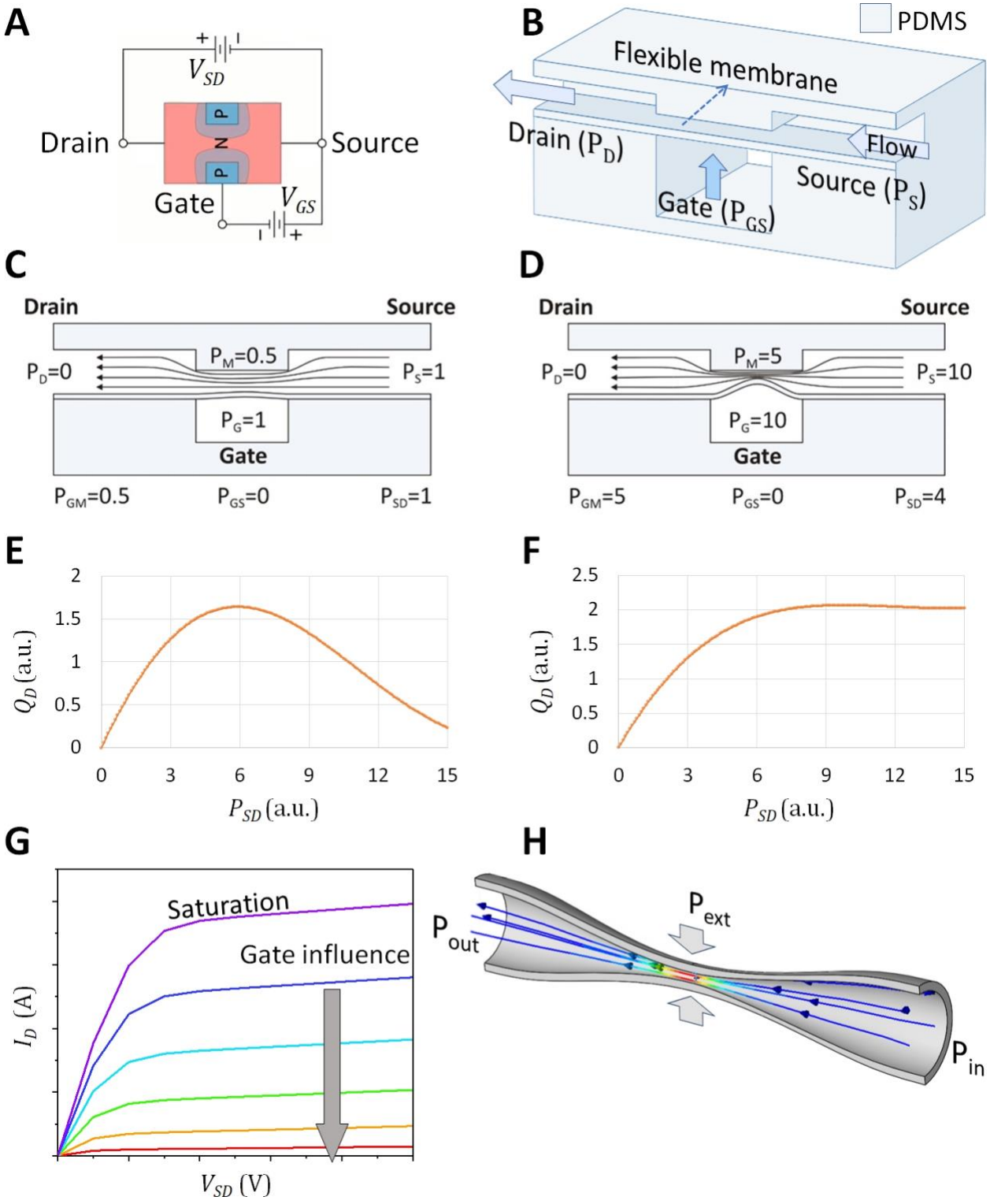

Fig. 1. Parallelism between saturation in electronic transistors and flow limitation in microfluidic transistors. (A) Cross-sectional schematic of a p-type field-effect transistor (FET) showing the source, drain, and gate areas. (B) Cut-away 3D schematic of a microfluidic PDMS analog of a FET featuring a PDMS membrane. The pressure driving the

flow in the channel is $\Delta P = P_S - P_D = P_{SD} > 0$. The membrane is actuated by the pressure differential $P_{GS} = P_G - P_S$ and the flow rate is modulated by the resulting membrane deflection. (C&D) Cross-sectional schematic of the transistor at low (C) and high (D) P_S values (a.u.), assuming the operating conditions of $P_{GS} = 0$ and $P_D = 0$. (E) Graph of Eqn. 1 for the case $k(P_{SD}) = k(0)$. (F) Graph of Eqn. 1 for the case $k(P_{SD}) = k(0) - (k(0)/40)\, P_{SD}$, which takes values $k(0)$ for $P_{SD} = 0$ and $0.6k(0)$ for $P_{SD} = 15$ psi. (G) Simulated graph depicting an ideal characteristic behavior of a FET and a microfluidic transistor. (H) Flow limitation phenomenon occurring in a flexible, collapsible tube upon applying pressures $P_{ext} \geq P_{in} \geq P_{out}$. The pressure driving the flow in the tube is $\Delta P = P_{in} - P_{out}$. Note that ΔP is always positive (both in the tube and in the channel), independently of whether the flow is driven by applying suction through the outlet/drain or by applying positive pressure to the inlet/source.

Higher-order analyses may produce similar predictions. Liu *et al*. have applied plane strain theory to describe large deformations of thin PDMS membranes, a formalism that could, in principle, be applied to build a more exact physical model of a microfluidic transistor.[52] Flow limitation was originally observed in compressible tubes (**Fig. 1**H) and was described theoretically, including non-linear second-order terms not considered above, by Shapiro[41,53,54] and others[55–59] (see section S1 in Supplementary Information). Shapiro's dimensionless analysis is also useful for predicting the occurrence of flow limitation. The dimensionless Shapiro number S combines the parameters of channel material properties, flow conditions, and the channel geometry, and predicts flow limitation when $S > 1$ (see section S2 in the Supplementary Information).[41]

2.b. Flow limitation and low hysteresis, the key ingredients for analog (proportional) amplification

Saturation is crucial to performing proportional amplification[51] and is a key behavior in any electronic transistor, used throughout circuit modern circuit design.[60,61] To show that, by analogy, flow limitation is a key behavior for performing proportional pressure amplification using microfluidic transistors (3D printed or not), we briefly explain here how a pressure amplifier works. (We demonstrate A 3D printed pressure amplifier below.) The description below is analogous to the well-known mechanism by which a common-source FET amplifier functions. To build a pressure amplifier, a microfluidic transistor is connected in series to a large resistive load such as a resistor or another transistor. The input pressure signal is fed into the gate and acts to change the flow passing through both the transistor and the series load. Due to the large load resistance,

minor changes in flow create substantial changes in pressure in the load. The output pressure signal is taken from the node between the two devices. Without flow limitation, the large changes in pressure at the output of the transistor would counteract the change in flow described above, preventing amplification. With flow limitation, the transistor has a high output impedance and behaves like a flow source that is independent of the high loads and pressure changes at the output, therefore allowing signal amplification. Critically, such a system can be shown to amplify only if the transistor acts sufficiently like a flow source with high output impedance (as it does in flow limitation) and can drive the large downstream resistive load.

The recent microfluidic transistor by Gopinathan *et al*.[41] used a normally open valve geometry (**Fig. 1**B) which operates as the fluidic analogy to a p-channel junction FET (p-JFET), mimicking its Q_D-P_{SD} saturation behavior (as conceptualized in **Fig. 1**G). As a voltage-driven device, the gate of an electronic p-JFET does not consume current, thus the gate does not contribute to I_D. Hence this transistor configuration is ideally suited to be "translated" to a microfluidic transistor because the fluidic gate can be pressurized in the absence of flow and there is no flow from the gate to the drain: in a valve, the impermeable membrane acts as a physical barrier between the fluid compartment controlling the gate and the fluid channel connecting to drain. (Note that flow limitation is based entirely on relative pressures between terminals.) Binary (on/off) valve configurations have been extensively used by many groups to construct microfluidic logic gates,[62–65] timers,[63,66] and oscillators.[66–68] However, for the device to function as an analog signal amplifier like the original electronic transistors (named after their transresistance gain[69]), binary switching is not sufficient. To achieve proportional amplification, the Q_D-P_{SD} relation must also mimic closely that of the I_D-V_{SD} in FETs.

Importantly, Gopinathan *et al*.[41] plotted the intrinsic gain (which quantifies the maximum proportional amplification achievable) and the flow-pressure characteristic curves (which are key for understanding how the transistor behaves under various operating conditions) of their transistor. They showed that the transistor's characteristic curves exhibited linear, cutoff, and saturation regimes and had a moderate intrinsic gain $g_0 = (dQ_D/dP_{GS})/(dQ_D/dP_{SD}) \gg 1$ (*i.e.*, suitable for proportional signal amplification), analogous to the current-voltage characteristics of a p-JFET.[41] We stress that the flatter the saturation curve, the higher the output impedance, and therefore the higher the intrinsic gain, g_0. Gopinathan's new transistors retained the capability of binary switching; hence they allowed for building transistor-based controls and circuit blocks such as logic gates in addition to analog amplification.[41]

Previously, others had 3D printed complex microfluidic valve networks to create digital logic[20,21] as well as fluidic controllers with larger feature sizes for robotic applications.[26–33] This prior work on microfluidic valves used deformable elastic structures to switch the flow of liquid on/off based on a small control pressure signal. This form of digital control led to considerable leaps in autonomous fluid processing and featured circuitry containing oscillators, logic gates, and other digital processing operations. However, most of these valves exhibit hysteresis,[70] in other words, the valves have some "memory" of their previous states and the threshold pressure to switch "on" differs from the threshold pressure required to switch "off". In some circuits, this behavior is desired, such as in flip-flops or debouncers. However, in most other circuit designs, hysteretic devices create fundamental problems in circuit function, since they produce unpredictable non-linear distortion based on their prior state and are insensitive to small signals that lie between the two thresholds. As a result of this non-linearity, in a device with hysteresis, an arbitrary signal (either electrical or fluidic) applied at the input will fail to produce a proportional signal at the output. Thus, hysteretic devices cannot be used as proportional amplifiers and are generally unsuitable for implementing circuits from analog electronics.

2.c. Multimaterial-SLA (mSLA) printed microfluidic transistors using cytocompatible, low viscosity, tunable blends of diacrylates and monoacrylates

Gopinathan *et al.*'s circuits,[41] including the transistors, were entirely fabricated in PDMS using conventional soft lithography, a technology that raises serious manufacturing concerns.[16] To address the manufacturing challenges of PDMS actuators, as a first approximation we sought to 3D print a polymer with properties matching or exceeding the mechanical properties of PDMS. (Note that our polymers are not siloxanes and thus we are only mimicking the mechanical properties of PDMS, not its molecular structure.) PDMS is a highly stretchable silicone elastomer (~140% elastic elongation) with a typical Young's modulus of ~0.5 MPa.[71] To replicate the PDMS transistors with SLA, a photopolymer is needed with elasticity and stretchability like PDMS and that can be 3D printed at high resolution. Most SLA-printable elastomers have some characteristics of PDMS (*e.g.*, similar Young's modulus) but they lack other properties (*e.g.*, stretchability, transparency), or they cannot be SLA-printed into high-resolution microfluidics features due to limited resin photo-reactivity.[42,48,72] The network structure of PDMS consists of high-M_w polymer segments (*i.e.*, long chains) between cross-links. Therefore, one approach to create PDMS-like polymers for SLA has been to use acrylated PDMS monomers.[42] However, these high-M_w monomers have a high viscosity, an undesirable feature because they are hard to remove from internal voids of microfluidic devices after the print process has ended, limiting the

smallest channel that can be achieved.[42] Another important consideration in working with viscous resins in SLA is that the suction force – which must be minimized to prevent distortion and delamination of layers – scales linearly with the resin's viscosity.

To overcome these challenges, we printed the actuator membrane using one of two photopolymer resins based on tunable blends of diacrylate and monoacrylate monomers, an approach that enhances the elasticity of the otherwise-rigid diacrylate print: either A) our previous blend of poly(ethylene glycol) diacrylate (PEGDA, M_w~258) and poly(ethylene glycol methyl ether) methacrylate (PEGMEMA, M_w~300) monomers, termed PEGDA-*co*-PEGMEMA;[48] or B) a copolymer blend of the 2-hydroxyethyl acrylate (HEA, M_w~116) and poly(propylene glycol) diacrylate (PPGDA, M_w~800), here termed HEA-*co*-PPGDA. Both resins were used in conjunction with 0.6 wt.% of photo-initiator Irgacure-819 and 0.6 wt.% of the photo-absorber 2-isopropylthioxanthone (ITX) (see Methods section). In these blends, tuning the monoacrylate to diacrylate ratio alters the elastic modulus of the printed plastics by over two orders of magnitude, reaching that of PDMS, while retaining the high transparency, high biocompatibility, and low drug absorption typical of the diacrylate, and offering a facile route for digital manufacturing not offered by PDMS molding.[48]

Both resin formulations, including the post-processing method, are highly cytocompatible, as compared to polystyrene controls and measured by the virtual absence of cell death in tissue cultures of Py8119 cells that were in direct contact with 3D printed wells for 24 hrs. These wells were 3D printed with the same size and shape as a single well of a 96-well well plate to ensure all cell cultures contained, by design, approximately the same number of cells and the same volume of cell culture medium. Live/dead staining (see Methods section) after 24 hrs of culture (**Fig. 2**A-C) showed high cell viability across all groups, with HEA-*co*-PPGDA and PEGDA-*co*-PEGMEMA supporting viability comparable to standard polystyrene 96-well substrates of the same well diameter (**Fig. 2**D). Quantification of morphological parameters such as individual cell area and cell aspect ratio (**Fig. 2**E-G) revealed no significant differences between cells cultured on HEA-*co*-PPGDA, PEGDA-*co*-PEGMEMA, and control polystyrene dishes. This consistent viability and morphology across different substrates (including the polystyrene control) suggests that our resin formulations and post-printing processing are very biocompatible, at least for the studied timeframe.

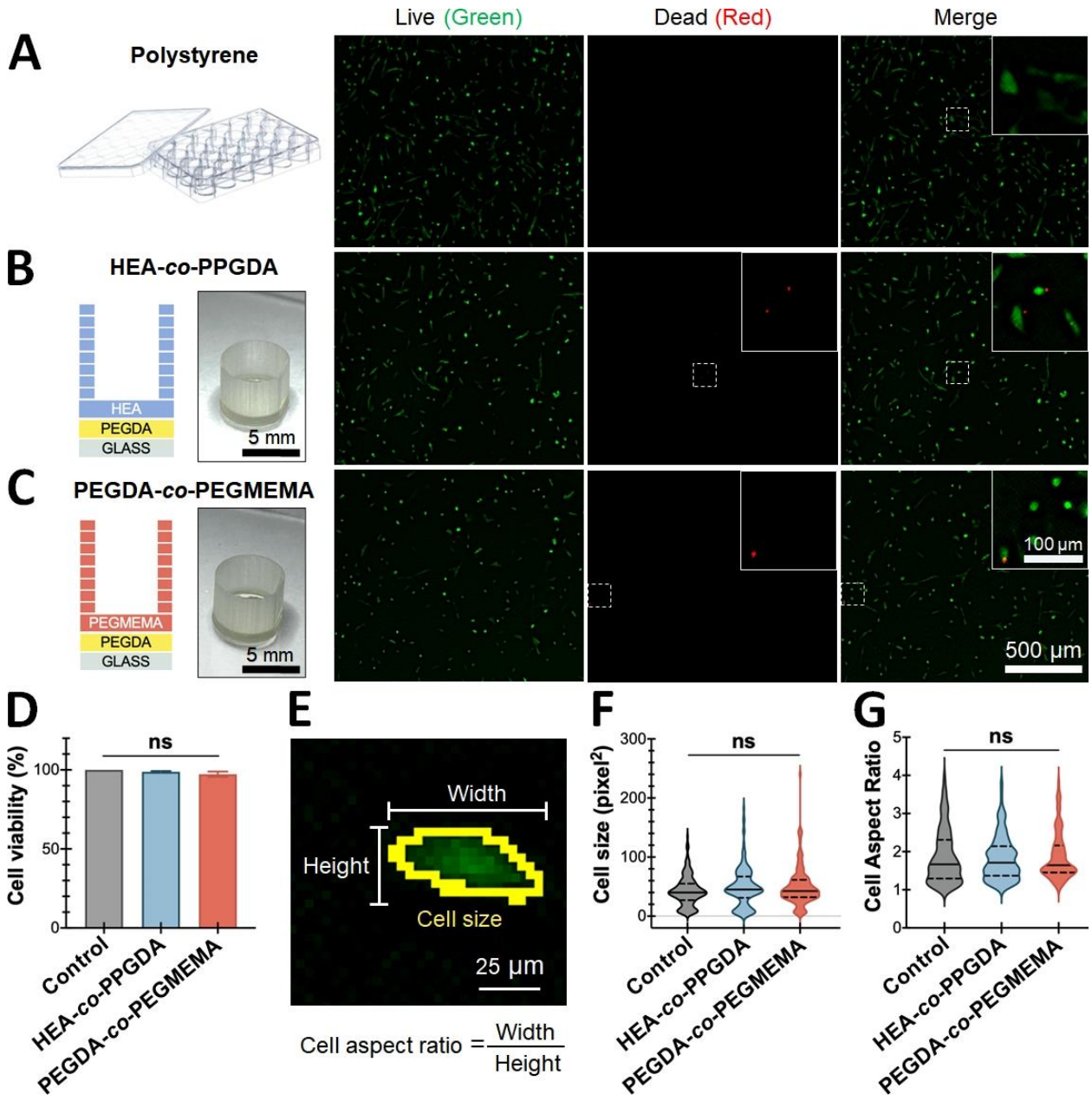

Figure 2. Comparison of Py8119 cells cultured for 24 hours in 3D-printed resin dishes versus standard polystyrene tissue culture dishes. 96-well polystyrene culture dishes (A) were compared to single-well 3D printed on glass substrates and coated with a PEGDA base layer using two resin formulations: HEA-*co*-PPGDA (B) and PEGDA-*co*-PEGMEMA (C). A schematic is shown on the left column (A-C) along with an image of a 3D-printed well (B,C). The fluorescence images in A-C show live cells (acridine orange (AO) staining, green, left column) and dead cells (propidium iodide (PI) staining, red, middle column) after 24 hrs of culture; the

rightmost column of images in A-C shows the merging of green and red channels. (D) Graph of green (AO-stained) cells as a percentage of total cells (red PI-stained and green AO-stained) for each condition. (E) Automated analysis of cell morphology, yielding cell size (area in pixel^2) and cell aspect ratio. (F) Cell size distribution for each condition. (G) Cell aspect ratio distribution for each condition. Statistical analysis indicated no significant difference (ns) among the three groups.

The microfluidic transistors were purposely designed with rigid walls and a flexible membrane, thus mandating the use of mSLA. While the microfluidic device could, in principle, be printed integrally in the same flexible material as the membrane, there are two important functional advantages for using mSLA to print a flexible membrane surrounded by a rigid body: a) leak-proof connections between outside flexible tubing are best achieved with (rigid) male barb connectors (Luer connectors are even better, but bulkier);[73] b) in a device with flexible walls, actuation of the membrane at high frequency results in a reduction in response time due to the high fluidic capacitance of the flexible walls of the control chamber and the rest of the device (*i.e.*, the energy used to displace the membrane is spent displacing not only the fluid but also the walls); this energy dissipation into the walls of the device does not occur when the walls are rigid.[74]

2.d. mSLA-printed microfluidic transistors with a PEGDA-co-PEGMEMA membrane

Our mSLA-printed microfluidic transistors with a membrane made of 40% PEGMEMA / 60% PEGDA (termed PEGDA-*co*-PEGMEMA) had high intrinsic gains. **Fig. 3**A shows the transistor's schematic with its three functional leads (the source, the drain, and the gate). Contrary to electrical devices that can have dead-end leads, 3D printed channels must have an inlet and an outlet, so the 3D printed device has 4 inlets (**Fig. 3**B), one of which is blocked during operation (**Fig. 3**B, inset, and **Fig. S**3). The transistor consists of a PEGDA-*co*-PEGMEMA membrane within a rigid PEGDA structure (see **Fig. 3**C schematic). Details of the "print-pause-print" multimaterial SLA-printing process of this hybrid structure are found in our previous work[48,49] as well as in the Methods Section. Note the single-pixel features in our prints (**Fig. 3**B inset), which are indicative of the highest-resolution that our printers can offer (27 μm). As illustrated in **Fig. 3**C and **Fig. S3**, when operating the microfluidic transistor, we apply a negative pressure P_D at the drain which pulls the flow from the transistor source. (Note that Gopinathan *et al*. applied positive pressure at the source to drive flow from source to drain; the choice of negative pressure for P_D to drive flow from source to drain for our studies is arbitrary, as the principle of flow limitation only depends on

the pressure difference. Therefore, the pressure difference between source and drain, P_{SD}, is always a positive quantity.) The gate-to-source pressure differential P_{GS} controlling the drain flow rate Q_D is applied to the membrane with respect to the source. By varying P_{GS}, we generated the full set of characteristic Q_D-P_{SD} curves of a SLA-printed microfluidic transistor featuring a 50 µm-thick PEGDA-*co*-PEGMEMA membrane, a 80 µm-high gate gap, and a PEGDA body with a 800 µm-wide fluid, 180 µm high channel (**Fig. 3**D). A contour plot of the intrinsic gain as a function of P_{GS} and P_{SD} for this microfluidic transistor is shown in **Fig. 3**E, demonstrating high gains of >40 when P_{SD} > 4 psi and P_{GS} ~ 0 psi. As indicated in **Fig. 3**D, we observe that our 3D printed microfluidic transistors replicate all three characteristics of a FET: linear (Ohmic), cutoff, and the saturation region.

While that changing the gap or the Young's modulus (by changing the %PEGMEMA composition), or both, in PEGMEMA-based transistors does not appreciably change the typical intrinsic gain (**Fig. S1**), we did observe a range of gains from transistor to transistor due to fabrication variability. The most critical element is the membrane, whose deflection is determined by the material (which is kept constant from one transistor to the next except for fluctuations in exposure) and by its thickness (see Eqn. 3 and its derivation in Supp. Info.). In our previous study by Kuo et al. we determined that, for PEGDA containing 0.6 wt.% of photo-initiator Irgacure-819 and 0.6 wt.% of photo-absorber ITX, the variability that we obtain in Z thickness for a light intensity of 85 mW/cm^2 (as in the present study) with our printer is about ~10 µm.[44]

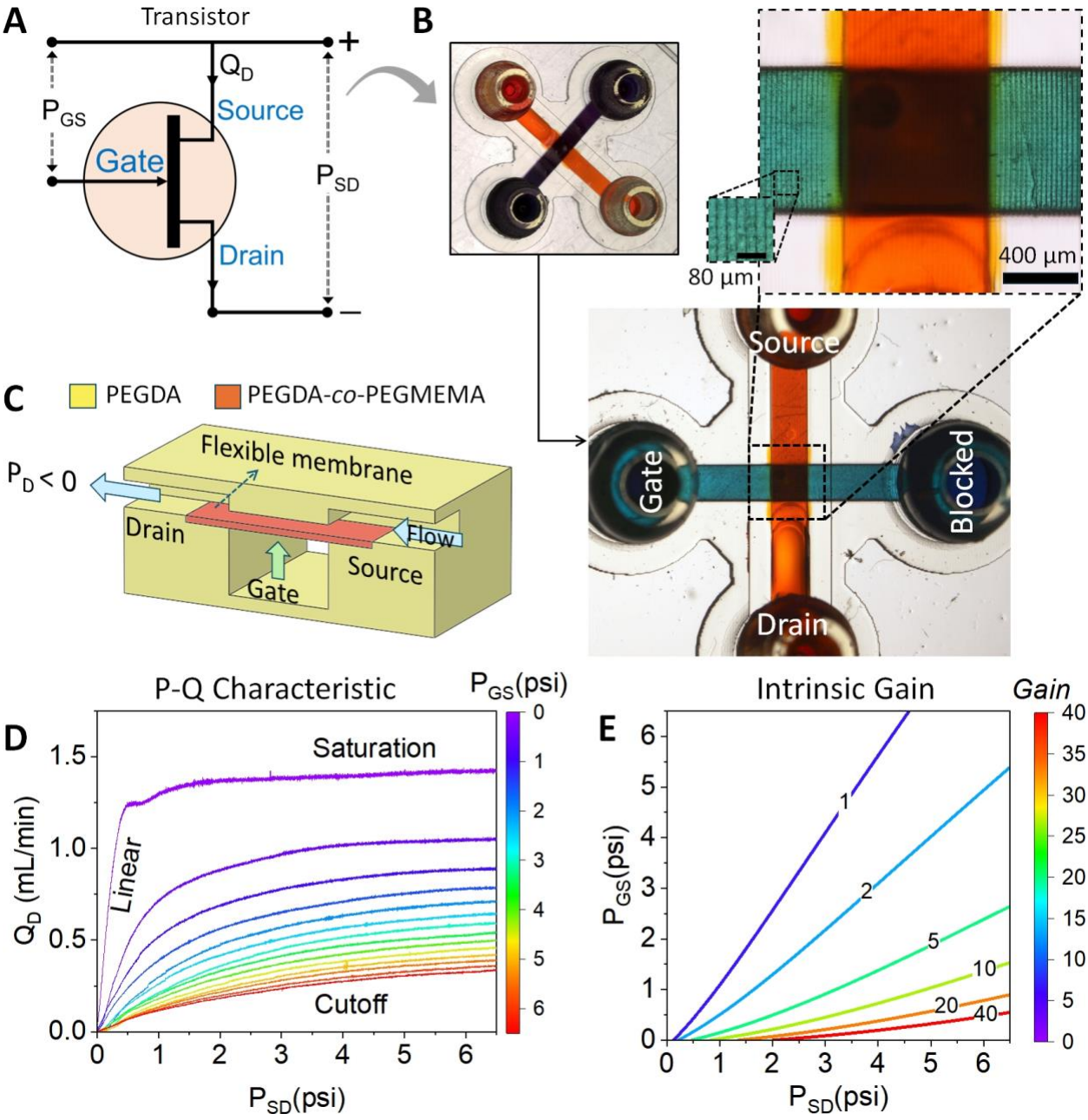

Figure 3. Microfluidic transistor printed with a PEGDA-*co*-PEGMEMA membrane using multimaterial SLA. (A) Schematic of a transistor depicting the three terminals (source, drain, and gate). (B) Photograph (top) and micrographs (bottom) of a mSLA-printed microfluidic transistor featuring a 50 µm-thick PEGDA-*co*-PEGMEMA membrane, an 80 µm-high gate gap, and a PEGDA body with an 800 µm-wide, 180 µm high fluid channel. The highest-magnification inset demonstrates that the PEGDA-*co*-PEGMEMA printing process has reached single-pixel (27 µm) resolution. (C) Cut-away 3D schematic of the multimaterial microfluidic transistor depicting the PEGDA body (yellow) and the PEGDA-*co*-PEGMEMA membrane (red). (D) Q_D vs

P_{SD} characteristic curve of a mSLA-printed microfluidic transistor (same dimensions as in B) illustrating a "linear" regime at low P_{SD} values, a "saturation" regime (where Q_D is nearly constant) at high P_{SD} values, and the "cutoff" point for P_{GS} ~6 psi (beyond which the gate interrupts all flow). (E) Contour plot of the intrinsic gain as a function of P_{GS} and P_{SD} for the microfluidic transistor shown in (D).

While, overall, PEGDA-*co*-PEGMEMA membranes produced excellent microfluidic transistors with intrinsic gains exceeding 40, reducing the number of cross-links in the polymer increased the brittleness of the membranes due to a weakened network structure. In other words, while the PEGDA-*co*-PEGMEMA material had the Young's modulus of PDMS, it fell short in elastic stretchability. This shortcoming can manifest itself in subtle ways. In high-cycle applications such as microfluidic logic, a non-stretchable material is particularly undesirable because it dissipates a lot of energy, *i.e.*, it presents high hysteresis during load and unload. While attempts to 3D print microfluidic transistors and amplifiers with PEGDA-*co*-PEGMEMA were successful, the large hysteresis of two-transistor amplifiers built in PEGDA-*co*-PEGMEMA confirmed that high stretchability is a critical material parameter for the performance of a microfluidic transistor not captured in the Shapiro number expression, which assumes a perfectly linearly elastic membrane material. Since the theory of flow-limitation assumes a linearly elastic membrane and does not predict hysteresis behavior,[54] we posited that the undesired hysteresis seen here is a result of irreversible deformation of the PEGDA-*co*-PEGMEMA membrane. When the PEGDA-*co*-PEGMEMA membranes are stretched beyond their elastic limit during the amplifier's forward sweep, they undergo permanent deformation and cannot return to their original shape when unloaded, as seen in the backward sweep. This behavior, known as viscoelastic hysteresis, occurs because the polymer's load-displacement responses differ between the loading and unloading phases, reflecting its inability to fully recover after being overstressed. Hence, we proceeded to replace the PEGDA-*co*-PEGMEMA blend resin with a more suitable blend resin.

The replacement for PEGDA-*co*-PEGMEMA resin is a blend of HEA and PPGDA (**Fig. 4**A) that uses the same photo-absorber (ITX) and the same photo-initiator (Irgacure-819) at identical concentrations (see Methods section), with no effect on cytocompatibility (see **Fig. 2**). We hypothesize that, in the HEA-*co*-PPGDA polymer network (**Fig. 4**B), HEA introduces reversible hydrogen cross-links, while the acrylate groups on both HEA and PPGDA form the stable cross-links.[75] Consistent with that hypothesis, the reversible cross-links increase the toughness and

elastic recovery of the polymer, an approach that is effective at modifying the mechanical properties of the polymer.[76,77] **Fig. 4**C shows how, by adjusting the ratio of reversible to stable cross-links through varying the HEA:PPGDA ratio in the resin, we can vary the tensile properties of the SLA-printed polymers. For instance, by increasing HEA concentration, the resulting polymer demonstrates lower Young's modulus and higher elongation, which we attribute to the increase in the number of reversible, hydrogen-bond cross-links in its network[77] (**Fig. 4**C). By carefully tuning the HEA:PPGDA ratio to 85% (v/v), the resulting resin can yield parts with similar Young's modulus and elongation to PDMS (**Fig. 4**D). We also measured the stretchability of 48 mm-long dog-bone prints (see **Fig. S**2) to compare various HEA:PPGDA ratios ranging 75% - 95% HEA; the maximum elongation ranged from ~80±6% (75% HEA) to ~126±19% (85% HEA) and ~220±13% (95% HEA) (**Fig. 4**D). While 95% HEA might appear a better choice on paper, in practice our target membrane sizes (800 μm-wide) resulted in 95% HEA membranes that sagged at zero applied pressure, making studies of Q_D vs P_{SD} difficult. Overall, compared to PDMS (stretchability ~155±10%), the 85% HEA resin demonstrated recoverable elastic properties that are best matched to PDMS, with ~19% less stretchability than PDMS, no sagging at zero applied pressure, and improved hysteresis (even slightly lower than PDMS) (**Fig. 4**E and **Fig. S**3).

Critically, these blends are SLA-printable at high resolution. We were able to SLA-print the 85% HEA resin into a 1 mm-wide unsupported 50 μm-thin layer (**Fig. 4**F) and pneumatically actuate 1 mm-diam. diaphragms of the same thickness at different pressures (**Fig. 4**G; note the peak deflections of ~375 μm and ~625 μm achieved at 4 psi and 8 psi, corresponding to a deformation 7.5 and 12.5 times its 50 μm thickness, respectively). The ability to 3D print these membranes is of central importance to the development of SLA-printed microfluidic actuators (transistors among them) whose function critically relies on membrane actuation without hysteresis. **Fig. 4**G and the **Video** in the Supplementary Materials show frame grabs and video sequences, respectively, taken at various time points along ~14 hrs of the repeated actuation of the membrane (~10,000 cycles) with a ramped pressure signal (0-8 psi) without any notable change in the membrane's dynamic behavior. This resilience of the membrane to sustain large, repeated deformations over so many cycles is consistent with the aforementioned hypothesis that the HEA-*co*-PPGDA polymer network contains a large number of reversible hydrogen-bond cross-links.[77]

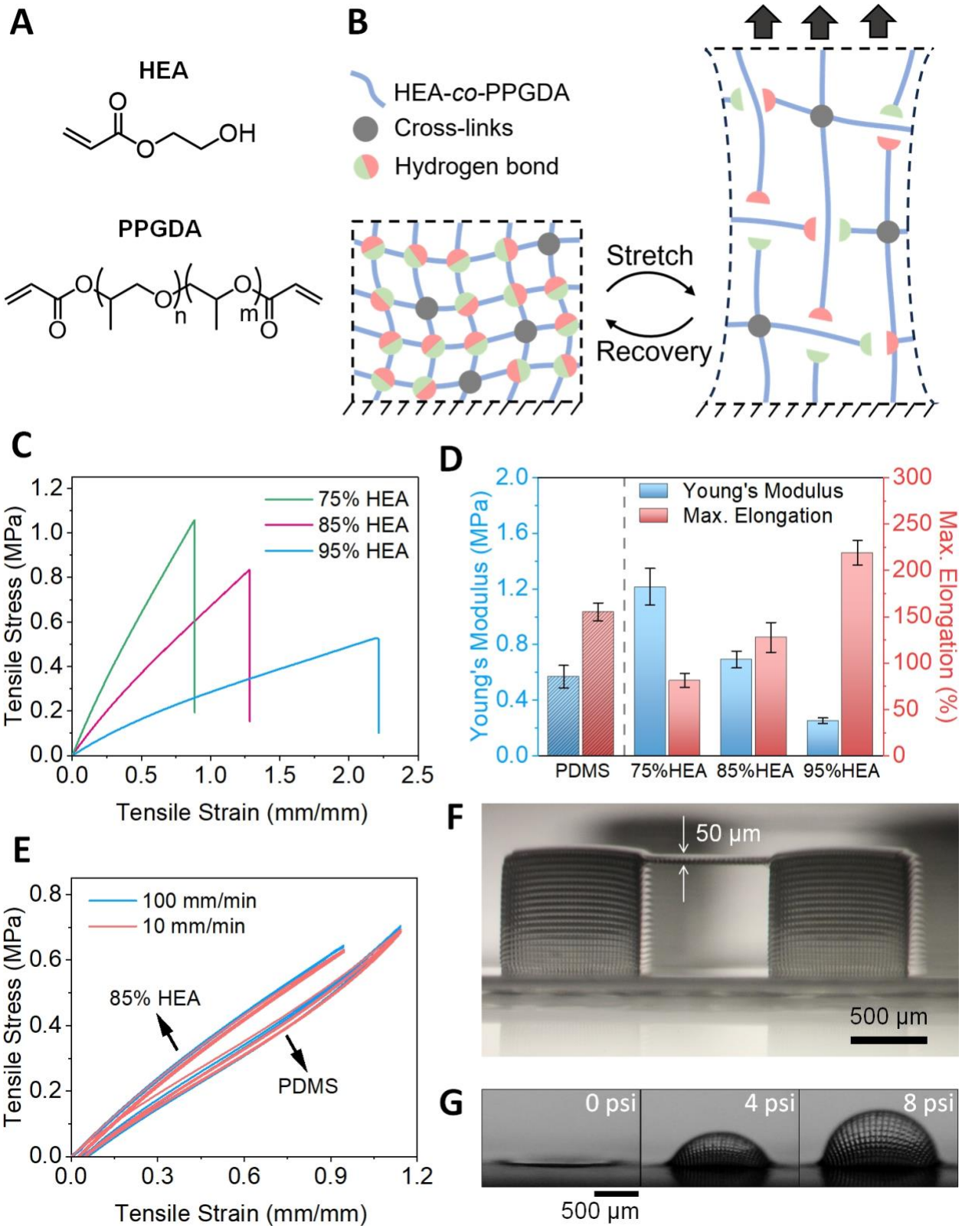
A
HEA
OH
PPGDA
B
HEA-co-PPGDA
Cross-links
Hydrogen bond
Stretch
Recovery
C
Tensile Stress (MPa)
Tensile Strain (mm/mm)
75% HEA
85% HEA
95% HEA
D
Young's Modulus (MPa)
Max. Elongation (%)
Young's Modulus
Max. Elongation
PDMS
75%HEA
85%HEA
95%HEA
E
Tensile Stress (MPa)
Tensile Strain (mm/mm)
100 mm/min
10 mm/min
85% HEA
PDMS
F
50 μm
500 μm
G
0 psi
4 psi
8 psi
500 μm

Figure 4. HEA-*co*-PPGDA photopolymer characterization. (A) HEA and PPGDA monomers. (B) Polymer network of HEA-*co*-PPGDA during stretch and recovery. (C) Tensile properties of HEA-*co*-PPGDA resins with various HEA contents. (D) Comparison of Young's modulus and maximum elongation of PDMS with HEA-*co*-PPGDA polymers with different HEA concentration. (E) Dynamic mechanical response of 85% HEA dog-bone specimen compared to that of a PDMS specimen of the same size. (F) Micrograph of an SLA-printed 1 mm-wide 85% HEA membrane (50 μm-thick) bridging two micropillars. (G) Micrographs of an SLA-printed 50 μm-thick 85% HEA membrane (1 mm dia.) actuated at different pneumatic pressures and 0.2 Hz frequency. See Movie in Suppl. Mater. The last micrograph in this sequence also demonstrates that the PPGDA-*co*-HEA printing process has reached single-pixel (27 μm) resolution.

To prove our hypothesis that undesired hysteresis in the PEGDA-*co*-PEGMEMA membrane is responsible for its failure to produce amplification in the initial microfluidic amplifier designs, we SLA-printed microfluidic transistors using 85% HEA resin. The transistor schematic is illustrated in **Fig. 5**A and a micrograph of a printed and fluid-filled transistor is shown in **Fig. 5**B. In this design, the transistor consists of an 85% HEA membrane within a rigid PEGDA structure. The inset micrograph in **Fig. 5**B shows that the printer is operating at single-pixel (27 μm) resolution. **Fig. 5**C demonstrates how the use of 85% HEA elastic membrane (E ~ 0.6 MPa) has led to the flow limitation in the microfluidic transistor in contrast to the rigid PEGDA membrane (E ~ 800 MPa). The observed flow limitation is controllable due to the reversible elasticity of the 85% HEA membrane, as shown in **Fig. 5**D. Note how the forward and backwards sweeps lie on top of each other, crucially indicating no hysteresis. If these elements had displayed hysteresis, they would not be capable of proportional amplification and would therefore be unsuitable for negative feedback controllers and, more generally, unsuitable for analog signal processing. It is important to note that the hysteresis behavior (or lack thereof) is not apparent in the Q_{SD} vs P_{SD} characteristic curves (**Fig. 5**E) or in the P_{GS} vs P_{SD} intrinsic gain curves (**Fig. 5**F). In this particular transistor (50 μm-thick 85% HEA membrane, 80 μm-high gate gap, 800 μm-wide fluid channel), there is a significant region of operation where the intrinsic gain exceeds 100 (for P_{SD} = 9 psi and P_{GS} = 1 psi), consistent with the very low slopes in the saturation regime close to cutoff in the Q_D-P_{SD} curves.

We next investigated whether digital manufacturing could be used to achieve geometries that would lead to improvements in intrinsic gain. Since we observed a substantial Q_D leakage flow

rate of ~60 μL/min at the cut-off P_{GS} = 9 psi (**Fig. 5**E), we implemented two 3D chamfers at the edge of the hydraulic microchannel (**Fig. 5**G&H). These 40 μm-tall and 40 μm-wide (slope = 45°) chamfers cannot easily be replicated by traditional microfabrication techniques such as photolithography, but we found that they play a crucial role in reducing the leak flow rate in the microfluidic transistors at the cut-off P_{GS}. After implementing the chamfers, the Q_D leakage flow rate sometimes became negligible (~2 μL/min at P_{GS} = 9 psi) (**Fig. 5**I). This feature suggests that our 3D microfluidic transistor can additionally function as a reliable switch with minimal flow leakage at closure. Importantly, because of the negligible slope in the saturation regime as seen in **Fig. 5**I, the intrinsic gain for this device became so high as to exceed what could be reliably measured. However, the variability in manufacturing (we estimate ~10 μm variability for the membrane thickness alone based on our previous results on PEGDA membranes[44]) can lead to large variations in the intrinsic gain, as shown in the three different P-Q characteristic curves (and the displayed gains) of **Fig. S4** measured for three additional chamfered transistors with the same exact design as the one in **Fig. 5**I. This result suggests the need for high-resolution 3D printers to achieve reliable flow limitation behavior in a manufacturing setting.

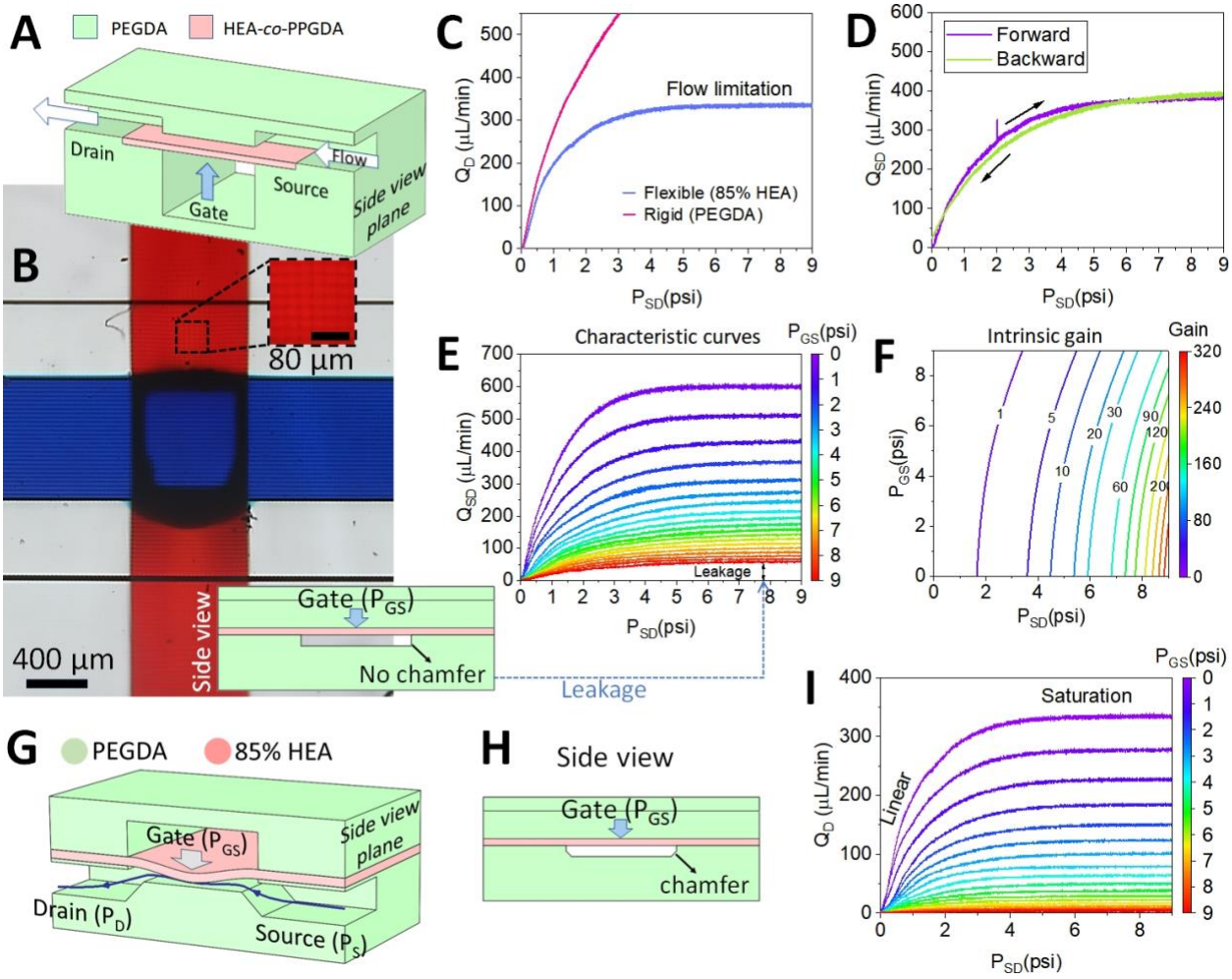

Figure 5. Performance of microfluidic transistors with mSLA-printed membranes in 85% HEA. (A) Cut-away schematic of a microfluidic transistor made in PEGDA (body, green) and 85% HEA (membrane, red). (B) Micrograph of a valve featuring an 85% HEA membrane with the flow channel filled with blue dye and the gate channel filled with red dye. The inset schematic depicts the side view, illustrating the lack of a chamfer in the cross section of the flow channel. (C) Comparison of flow limitation in SLA-printed microfluidic transistors made with an 85% HEA membrane (blue) or PEGDA (red), showing that a highly flexible material is required for this measurement. (D) Forward and backward sweep of P_{SD} at P_{GS} = 0 for the SLA-printed microfluidic transistor with a 50 µm-thick membrane made of 85% HEA. (E,F) Q_D-P_{SD} characteristic curves (E) and contour plot of the intrinsic gain as a function of P_{GS} and P_{SD} (F) of a mSLA-printed microfluidic transistor with a 50 µm-thick 85% HEA membrane and 80 µm gate gap in the absence of chamfers; the leakage flow is indicated with a blue dashed arrow in (E). Note that, for this transistor, the peak intrinsic gain is 320 when P_{SD} = 9 psi and P_{GS} = 1 psi. (G-I)

The implementation of chamfers (40 μm height × 40 μm width) in the design shown in (G) and (H) helps the membrane conform to the edges and virtually eliminates leakage (I).

To demonstrate analog pressure amplification, we tested the performance of a mSLA-printed common-source amplifier. This design generates pressure gain by operating two transistors in unison (in series) (**Fig. 6**). The amplifier circuit design mimics a common-source voltage amplifier with active load (**Fig. 6**A). (Note that this design inverts P_{out} with respect to P_{in}.) A top-view schematic of its fluidic analogue is shown in **Fig. 6**B. Similarly to the single-transistor circuit, we printed an extra inlet to be able to flush the uncured resin and facilitate the filling of the transistor with fluids, but during operation this inlet was blocked (**Fig. S**5). The hydraulic resistances R_{h1} and R_{h2} are ~36×10^{-7} psi.μL/min, imposing negligible pressure loss between the two transistors, and the supply pressure for the typical range of Q_D less than 1000 μL/min. One characteristic feature of this type of circuit is that, if the two transistors are not identical in performance, the circuit's gain becomes *lower* than the intrinsic gain of either transistor (see Discussion).

The performance of the amplifier circuits was strikingly different depending on the resin employed to print the actuator membrane. For amplifier circuits printed with PEGDA-*co*-PEGMEMA membranes, each of the transistors had Q_D-P_{SD} characteristic curves like that in **Fig. 3**D and an intrinsic gain in excess of 40. Unfortunately, the amplifier circuit did not achieve the performance predicted by the intrinsic gain of the transistors alone, indicating a mismatch in performance. Moreover, while one amplifier's transfer curve (**Fig. 6**C) showed almost 5x changes in output pressure (~2.93 psi) with small changes in input pressure (~0.61 psi), all amplifiers built with PEGDA-*co*-PEGMEMA membranes displayed significant hysteresis (**Fig. 6**D) as seen by the different threshold pressures when sweeping the input pressure from low to high (orange) and high to low (green). Such a device would be suitable for making flip-flops and Schmitt triggers but would not be suitable for proportional amplification since, due to hysteresis, the output signal is not purely proportional to the current input signal and is instead influenced by the "memory" of its prior states.

Amplifiers printed with 85% HEA-*co*-PPGDA membranes (**Fig. 6**E), on the other hand, did not show the hysteresis of their PEGDA-*co*-PEGMEMA counterparts. The first (top) transistor was a chamfered transistor and operated according to the Q_D-P_{SD} curves in **Fig. 5**I, accepting the input pressure signal P_{in}. The second (bottom) transistor was printed with the same parameters (50 μm-

thick 85% HEA membrane, 80 μm gate gap, no chamfers, and 800 μm-wide, 180 μm high fluid channel) and acted as an active load to enhance the amplifier gain by operating as a constant flow source (again using flow limitation). To evaluate the amplifier's performance, we first swept P_{in} between 1.0 to 2.5 psi (being the approximate operating range of the amplifier) and monitored P_{out}. The transistor demonstrated no significant hysteresis in producing an amplified output pressure between ~3 and 7.5 psi (**Fig. 6**F). The lack of hysteresis is critical in preserving the shape of the input signal and allowed for proportional amplification. **Fig. 6**G depicts the output response of the microfluidic amplifier when the input signal is of a sine type. As shown, the circuit amplified the pressure signal by a gain of ~4 with a sinusoidal output waveform that closely follows the input waveform. As expected from imperfectly matched transistors, this demonstration of amplification is much lower than the maximum set by the transistor's intrinsic gain, which is a theoretical maximum gain for the best 1-transistor amplifier one could ideally construct with a given P_{GS} and P_{SD} (see Discussion).

Some degree of clipping when operating the transistor outside of saturation is expected in any common-source amplifier (including in electronics) and can be observed in **Fig. 6**G. When the input pressure signal is too high (at the peaks of the red sinusoid in **Fig. 6**G), the top transistor experiences high P_{GS}, exiting saturation and entering the cutoff regime. As seen in the upper region of **Fig. 5**F (high P_{GS}), this area of operation has low intrinsic gain, so amplification does not take place. Similarly, if the input pressure signal were too low, the top transistor would experience low P_{SD} and would exit saturation and enter the linear regime. As seen in the left region of **Fig. 5**F (low P_{SD}), this area also has a low intrinsic gain and so would again block amplification. This behavior highlights the importance of transistor saturation in the proper functioning of all these circuits. In electronics, designing the circuit to ensure that all transistors operate in the appropriate regime is known as "biasing" and is a major part of all transistor circuit design.

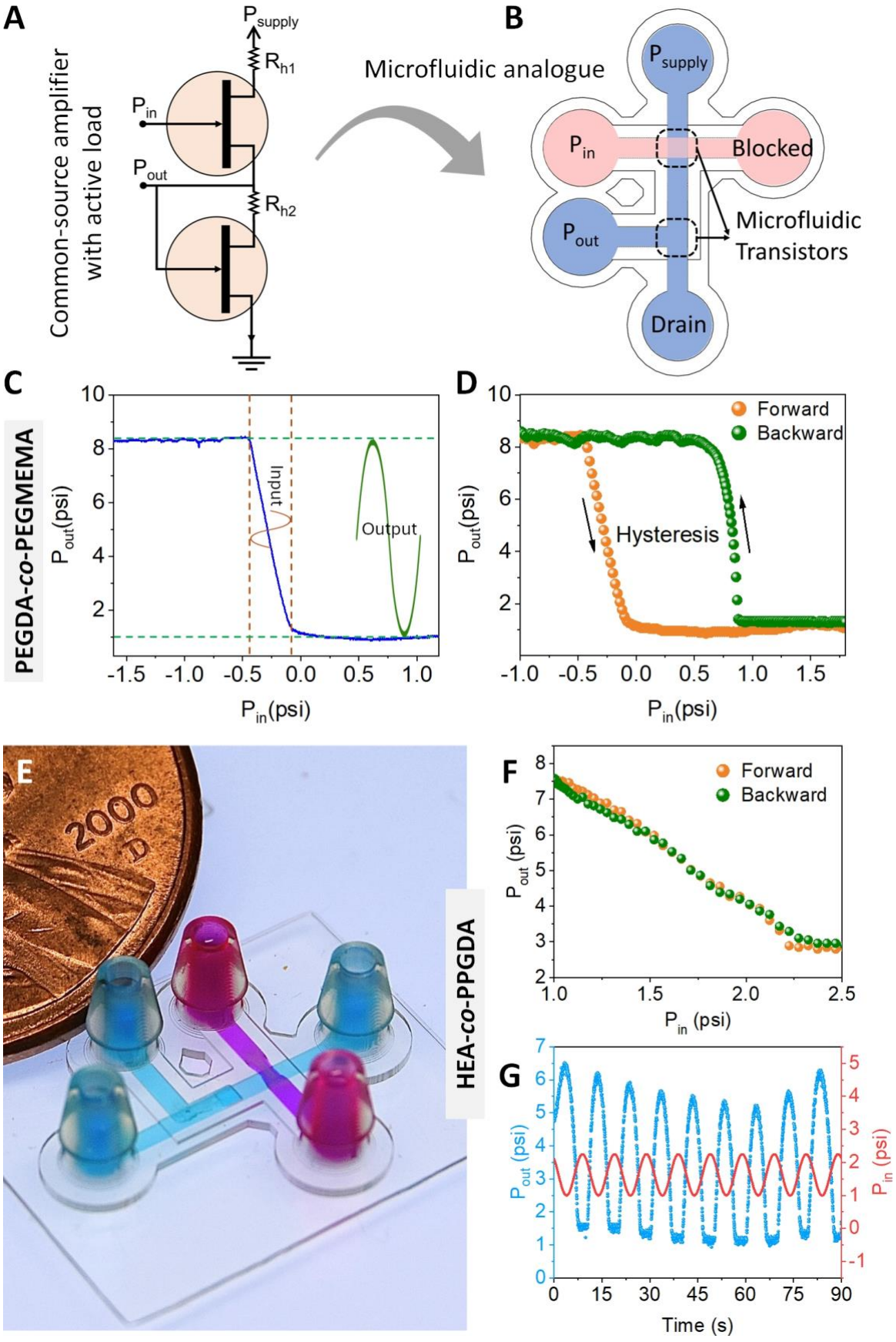
A
Common-source amplifier with active load
P_supply
R_h1
P_in
P_out
R_h2
Microfluidic analogue
B
P_supply
P_in
Blocked
P_out
Microfluidic Transistors
Drain
C
PEGDA-co-PEGMEMA
P_out(psi)
Input
Output
P_in(psi)
D
Forward
Backward
Hysteresis
P_out(psi)
P_in(psi)
E
HEA-co-PPGDA
F
Forward
Backward
P_out (psi)
P_in (psi)
G
P_out (psi)
P_in (psi)
Time (s)

Figure 6. Microfluidic amplifiers printed using multimaterial SLA. (A) Electrical circuit and its microfluidic analogue (B) of a common-source analog amplifier with active load. (C) Transfer characteristic of a 3D-printed PEGDA-*co*-PEGMEMA amplifier showing an example of input sine wave excitation versus the sine wave output (expected). (D) Hysteresis characterization of the PEGDA-*co*-PEGMEMA amplifier in (C) by comparing how P_{out} varies with the forward and backward sweep scans of the input pressure P_{in}. (E) Image of an SLA-printed 85% HEA membrane amplifier filled with pink (pneumatic microchannel) and blue (hydraulic microchannels) dyes for visualization. (F) Transfer characteristic of the HEA-*co*-PPGDA analog amplifier in (E), showing absence of hysteresis. (G) Input (P_{in}) versus output (P_{out}) pressure of the HEA-*co*-PPGDA analog amplifier in (E).

3. Discussion

The novelty of our work is that we have achieved 3D-printability of a microfluidic transistor design that could pave the way for more sophisticated, integrated on-chip automation, similarly to how FETs enabled complex control in microelectronics.[41] To disseminate this technology, a rapid, versatile, and scalable manufacturing technique is needed, which is beyond the capabilities of soft lithography. Nevertheless, we recognize that the digital manufacturing of autonomous microfluidic circuits with a complexity similar to that of electronics is still far away. We chose acrylate photopolymer resins because of their proven speed, high resolution, and biocompatibility. Here we have focused on the short-term characterization of HEA-*co*-PPGDA in terms of biocompatibility, elasticity, stretchability, and suitability for high-precision 3D printing (minimal viscosity, SLA suction force, etc.). Note that, in principle, for a given Young's modulus E, flow limitation can be reached by altering dimensional parameters that greatly affect the shape of the Q_D-P_{SD} curves, such as the membrane thickness t or the length L, width ω, or height H of the valve (see Eqn. 3 and Suppl. Info.). In practice, however, for our 3D printer (max resolution 27 μm), we found that a highly stretchable elastomeric resin is needed to obtain a low-hysteresis amplifier that replicates the mechanical properties of PDMS. Higher-resolution 3D printers that allow for exploring smaller dimensions might be more forgiving with the membrane materials.

A limitation of our design is that the flow-pressure characteristic of any analog transistor is extremely sensitive to its geometry (see Eqn. 3). While we measured intrinsic gains of over 300

in individual transistors, due to mismatches in geometry during manufacturing we could only demonstrate single-digit gains (4 and 9) when we connected two transistors in an amplifier. When the transistor is actually used to build an amplifier, the amplifier's gain will be lower due to non-idealities in the power source, noise, and manufacturing. In the common-source amplifier design demonstrated here, the maximum gain is achieved when the two transistors are perfectly matched in their flow-pressure characteristics, so that the total gain of the amplifier is equal to the intrinsic gain of the individual transistors that make it up. The highest achievable pressure amplification in our amplifier circuit is affected by several sources of errors including dissimilarity between the two transistors and existing parasitic capacitances in the experimental setup and measurement. The dissimilarity stems from morphological differences in the 85% HEA membrane that are typical in 3D printing of elastic thin membranes.[48] We have previously observed a variability in the thickness of 3D printed PEGDA membranes as large as 10 μm.[44] Additionally, formation and accumulation of air bubbles in conjunction with the air in our reservoir bottles (see **Fig. S**6 for a schematic of the amplifier setup) introduce parasitic capacitances that can diminish the amplifier gain by absorbing pressure increase at P_{out} or P_{in}. Unfortunately, the above error sources prevented our transistors from matching perfectly, with the bottom transistor saturating at a lower flow rate than the top transistor. This behavior forced the top transistor to operate closer to the cutoff regime and severely reduced the overall gain of the circuit.

We conclude that circumventing the above limitation will require high-resolution 3D printers. The fact that the amplifier's gain is still far from the intrinsic gain of the individual transistors means that there are many opportunities for future manufacturing improvements in 3D printed membranes and the resulting microfluidic transistors and amplifiers. We believe that the gain reduction we observe in amplifier circuits when its transistors' performances are not well matched could be used to establish mSLA manufacturing milestones in the future. Undoubtedly, one of the next frontiers will be on reliable manufacturing to obtain high amplification in more complex devices, which will require higher-resolution SLA printers. Our 3D printer's resolution (27 μm projected XY pixel size) and build size (7.1 cm x 4 cm) allows for footprints that fit only a few transistors, however that number is presently a limitation for the production of larger circuits.[51] Complex fluidic controls such as timers and oscillators or op-amps (typically featuring tens of hundreds of transistors in electronics[51]) necessitating larger numbers of transistors will require more advanced, next-generation 3D printers (such as those based on 8K projectors or 2-photon SLA technology) with larger build sizes.

Further studies should also investigate factors influencing the long-term performance of the transistors, including durability and long-term stability, which can depend on storage conditions. Most importantly, their scalability (*i.e.*, repeatability and modularity), which is strongly dependent on the printer, must be assessed. A challenge for standardization will be the long-term quality of the resins – acrylate resins are sensitive to temperature and humidity,[78] so the elasticity, stretchability, and the biocompatibility of the membranes may change depending on their storage conditions. Long-term cytocompatibility and chemical stability under continuous fluid perfusion were not tested in this study and represent an important area for future investigation, especially for organs-on-chips applications. We conclude that implementing microfluidic transistors for automation of room-temperature/benchtop biomicrofluidic applications such as bioassays will be significantly simpler to achieve than in applications that demand incubation in the presence of cells or tissues for extended periods of time, *e.g.*, organs-on-chips. In the short term, temperature sensitivity can foreseeably be addressed with designs where the microfluidic transistors are placed in a separate module just outside the incubator. If needed, the cytocompatibility of SLA-printed surfaces can be increased with biocompatible resins,[79] thorough rinsing,[44,80] and/or parylene C coatings.[81]

Our work extends the capabilities of 3D printed microfluidic circuitry to perform both analog and digital signal processing, which has numerous benefits. Firstly, it enables the direct translation of a broad class of analog circuit designs from the electronics literature, including power converters, regulators, references, active filters, analog-to-digital/digital-to-analog converters, and many others. Secondly, it enables the creation of negative feedback controllers, which is a ubiquitous motif in high-performance circuit designs, where precision and speed are of utmost importance and digital systems suffer from quantization error.[51,61] This error is potentially acute in microfluidics, where the pressures and flows involved are very small and require tight control, such as when moving a single cell[41] or tuning flow resistances.[82] Last but not least, in microfluidics real estate tends to be more critical than in microelectronics. Until microfluidic fabrication becomes capable of placing hundreds of thousands of transistors on a chip, analog circuits will be more economical in space and transistor count when performing the same operations as their digital counterparts.[83,84]

In summary, SLA offers several critical features that we believe will significantly advance the manufacturing of advanced 3D printed microfluidics containing transistors: (*i*) monolithic fabrication of the entire fluidic circuits eliminates the need for aligning, bonding, and fabricating circuit interconnects and inlet/outlet ports, significantly streamlining the circuit fabrication and

experimental implementation; (*ii*) the rapid-prototyping of fluidic circuits via SLA (or mSLA) considerably improves the circuit design verification by allowing multiple design iterations at a fraction of the time, cost and labor; (*iii*) the simplicity of fabricating 3D architectures by SLA potentially enables the printing of out-of-plane transistors,[85,86] hence the production of microfluidic circuits with much higher density of transistors, *i.e.*, higher processing power; and (*iv*) the presence of SLA machines in many laboratories around the world or in the form of 3D printing commercial services effectively 'democratizes' the implementation of 3D printed microfluidics without access to high-end facilities. Moreover, our HEA-*co*-PPGDA resin formulation enables the digital fabrication of low-hysteresis microfluidic transistors that closely replicate key field-effect transistor behaviors, including saturation and proportional amplification. As printer resolution, material uniformity, and manufacturing reproducibility continue to improve, this approach could support dense, reliable microfluidic circuits capable of analog signal processing, feedback control, and autonomous operation (*e.g.*, timers[66,87] and oscillators[66,67]) to meet the automation demands of complex microfluidic systems. Ultimately, these advances point toward a future in which microfluidic control architectures can be designed, fabricated, and iterated with an agility analogous to that which enabled the rise of modern electronics.

4. Methods

4.1. Resin formulation

PEGDA resin is prepared by mixing poly(ethylene glycol) diacrylate (PEGDA, M_w~258, Sigma-Aldrich) with 0.6 wt.% phenylbis (2,4,6-trimethylbenzoyl) phosphine oxide (Irgacure-819, BASF, IL) as the photo-initiator and 0.6 wt.% 2-isopropylthioxanthone (ITX) (PL Industries, PA) as the photo-absorber. PEGDA-*co*-PEGMEMA resin is prepared by mixing 40 wt.% PEGMEMA with 60 wt.% PEGDA, and then mixing with 0.6 wt.% of Irgacure-819 and 0.6 wt.% of ITX. HEA-*co*-PPGDA resin is prepared by mixing a known volumetric ratio (depending on the experiment) of 2-hydroxyethyl acrylate (HEA, M_w~116, Sigma-Aldrich) and poly(propylene glycol) diacrylate (PPGDA, M_w~800, Sigma-Aldrich) with 0.6 wt.% of Irgacure-819 and 0.6 wt.% of ITX.

4.2. Measurement of elastic properties

To measure the elastic properties of HEA-*co*-PPGDA printed polymers, we have printed SLA-printed dog-bone specimens (**Fig. S2**a) and measured their tensile properties according to ASTM (D638-10) standard. Similarly, PDMS dog-bone specimens were prepared by molding Sylgard 184 (1:10 curing ratio). We used Instron 5584H load frame equipped with a 50 N load cell (**Fig. S2**b). The extension rate of the specimen was set at either 10 or 100 mm/min depending on the experiment, and the elongation was recorded with a video extensometer. The dynamic mechanical responses of 75% and 95% HEA are given in **Fig. S3** of the Supplementary Information.

4.3. SLA-printing process

The microfluidic transistors and amplifiers have a hybrid structure combining an elastic HEA-*co*-PPGDA membrane and a rigid PEGDA structure. These hybrid structures were SLA-printed using a “print-pause-print” protocol, as in our previous works.[48,49] We used a digital light projection (DLP) SLA 3D printer (Pico 2 HD, Asiga) that has a X-Y pixel resolution of 27 µm, equipped with a 385 nm UV-LED light source. In our prints, we set the light intensity at 85 mW/cm^2. To SLA-print microfluidic transistors and amplifiers, we used a glass slide attached to the 3D printer’s build platform. Prior to 3D printing, the glass slide is washed successively with acetone, IPA, and DI-water, and dried in an oven at 80 °C for 20 min. The glass slide is finally silanized with 3-(trimethoxysilyl)propyl methacrylate (Sigma-Aldrich) overnight to ensure the attachment of polymerized resins onto its surface, according to our previously published protocol.[45] To attach the glass on the build platform, we used a drop of PEGDA resin followed by curing under ambient

light for ~5 min. To detach the glass slide from the build platform after the print, we wedged a razor blade between the build platform and the glass slide. After the print, the microfluidic devices were immersed in IPA bath for ~20 min away from ambient light. Then, we flushed the microchannels with IPA to completely remove uncured resin. After the parts are dried in ambient air, we then placed them under a UV light source for ~1 min to completely cure the resin remaining on the walls. The STL files for microfluidic transistors and amplifiers are available in the Supplementary Information.

4.4. **Cell culture and post-processing procedure for fluorescent cell staining**

Using both resin formulations, we printed single-well culture dishes on PEGDA-coated glass substrates; these 3D printed single wells were of the same size and shape as a single well of a 96-well well plate. Immediately after printing, the constructs underwent a standardized post-processing protocol: (1) immersion in isopropanol (IPA) for 2 hrs in the dark, (2) flushing with fresh isopropyl alcohol (IPA) and deionized water to remove unreacted monomers and prevent microchannel blockage, (3) air drying, (4) UV curing for 1–2 min to complete polymerization and enhance structural stability, and (5) thermal treatment at 70 °C for 30 min to terminate the photoreactants. Prior to cell seeding, the devices were pre-soaked in culture medium, rinsed with PBS, and seeded with Py8119 cells at a concentration of 0.07×10^6 cells per well. The Py8119 cell line is a mesenchymal-like cell line that was originally derived from a mammary adenocarcinoma that spontaneously arose in a C57BL/6 female mouse with the MMTV-PyMT transgene. Since Py8119 are used to assess cytotoxicity in cancer treatments, here we used them to measure whether our resins had any cytotoxic effects. Acridine Orange (AO, 2 μg/mL) and Propidium Iodide (PI, 1 μg/mL) were added directly to the culture medium after 24 hrs of culture to generate AO/PI staining. The mechanism of imaging with acridine orange (AO) and propidium iodide (PI) relies on the differential membrane permeability of the two dyes, enabling the distinction between live and dead cells based on their fluorescence. AO is a small, cell-permeable dye that can cross the intact membranes of both live and dead cells, whereas PI is a larger dye that is impermeable to the membranes of live, healthy cells. Once AO is inside the cell, it binds to nucleic acids (DNA and RNA). When bound to double-stranded DNA (dsDNA) inside cells, AO emits green fluorescence when excited with blue light. PI, on the other hand, can only enter cells with compromised or damaged membranes, a characteristic of dying, dead, or necrotic cells. PI also binds to nucleic acids inside the cell, but emits a strong red fluorescence. The combination of these dyes in a single solution allows for simultaneous live and dead cell assessment. Live cells fluoresce green because only AO can enter live cells. Dead cells, on the other hand,

fluoresce red because, due to Fluorescence Resonance Energy Transfer (FRET), the green fluorescence emitted by AO is absorbed by the nearby PI molecules, and only the red fluorescence of PI is observed.[88] Fluorescence images were acquired using an exposure time of 1/35 s for the green channel (AO) and 1/20 s for the red channel (PI).

4.5. **Microfluidic setup**

The microfluidic transistor and the microfluidic pressure amplifier were tested according to the setup shown in **Fig. S4** and **Fig. S5**, respectively. The input pressure to the transistors and amplifiers was generated with a pressure controller unit (Elveflow). To measure the output flow rates, we used a flow sensor (Sensirion). To calculate the pressure output (P_{out} in **Fig. S5**) of the amplifier, we used a differential pressure sensor (Honeywell).

Supporting Information

The following Supporting Information is available online: Alternative expression for the Shapiro number *S*; Variability in P-Q characteristic curves and intrinsic gain for various PEGDA-*co*-PEGMEMA transistors of different membrane composition and gap height; Dynamic mechanical response of HEA-*co*-PPGDA; Variability in P-Q characteristic curves and intrinsic gain for various PPGDA-*co*-HEA transistors of exact design dimensions; Schematics of the experimental setup for testing microfluidic transistors and analog pressure amplifiers; Video of the 85% HEA membrane periodic actuation; STL design files for microfluidic transistors and amplifiers.

Acknowledgments

A.F. acknowledges partial financial support from the National Institute of General Medical Sciences (R21GM137161) and the National Cancer Institute (2R01CA181445). M.T. acknowledges partial financial support from the National Institutes of Health (U01CA268933 and R01CA255602). T.-Y.T. acknowledges partial support by the National Science and Technology Council (NSTC), Taiwan (NSTC 113-2314-B-006-094-MY3, NSTC 112-2628-B-006-014-MY3), and by the Higher Education Sprout Project, Ministry of Education to the Headquarters of University Advancement at National Cheng Kung University.

Author contributions (alphabetical order)

Conceptualization: AA, AF, KAG, MT
Methodology: AA, AF, KAG, LH, WH
Investigation: AA, AF, IS, KAG, WH
Formal Analysis: AA, AF, KAG, TYT, WH
Data Curation: AA, AF, IS, WH

Supervision: AF, LH, MT, TYT
Writing—original draft: AA, AF, KAG, MT
Writing—review & editing: AA, AF, IS, KAG, LH, MT, TYT, WH

Competing interests

The authors declare no competing financial interest.

References

1. Hong, J. W., Studer, V., Hang, G., Anderson, W. F. & Quake, S. R. A nanoliter-scale nucleic acid processor with parallel architecture. *Nat Biotechnol* 22: 435–439 (2004).
2. Liu, J., Enzelberger, M. & Quake, S. A nanoliter rotary device for polymerase chain reaction. *Electrophoresis* 23: 1531–1536 (2002).
3. Gerber, D., Maerkl, S. J. & Quake, S. R. An in vitro microfluidic approach to generating protein-interaction networks. *Nat Methods* 6: 71–74 (2009).
4. Garcia-Cordero, J. L. & Maerkl, S. J. A 1024-sample serum analyzer chip for cancer diagnostics. *Lab Chip* 14: 2642–2650 (2014).
5. Pang, L., Liu, W., Tian, C., Xu, J., Li, T., Chen, S. W. & Wang, J. Construction of single-cell arrays and assay of cell drug resistance in an integrated microfluidic platform. *Lab Chip* 16: 4612–4620 (2016).
6. Leung, C. M., de Haan, P., Ronaldson-Bouchard, K., Kim, G. A., Ko, J., Rho, H. S., Chen, Z., Habibovic, P., Jeon, N. L., Takayama, S., Shuler, M. L., Vunjak-Novakovic, G., Frey, O., Verpoorte, E. & Toh, Y. C. A guide to the organ-on-a-chip. *Nature Reviews Methods Primers* 2: 33 (2022).
7. Zhang, C., Tu, H. L., Jia, G., Mukhtar, T., Taylor, V., Rzhetsky, A. & Tay, S. Ultra-multiplexed analysis of single-cell dynamics reveals logic rules in differentiation. *Sci Adv* 5: eaav7959 (2019).
8. Gomez-Sjoberg, R., Leyrat, A. A., Pirone, D. M., Chen, C. S. & Quake, S. R. Versatile, fully automated, microfluidic cell culture system. *Anal Chem* 79: 8557–8563 (2007).

9. Hoffman, J. M., Ebara, M., Lai, J. J., Hoffman, A. S., Folch, A. & Stayton, P. S. A helical flow, circular microreactor for separating and enriching ‘smart’ polymer-antibody capture reagents. *Lab Chip* 10: 3130–3138 (2010).

10. Hsu, C. H. & Folch, A. Spatio-temporally-complex concentration profiles using a tunable chaotic micromixer. *Appl Phys Lett* 89: 144102 (2006).

11. Lee, K. K., McCauley, H. A., Broda, T. R., Kofron, M. J., Wells, J. M. & Hong, C. I. Human stomach-on-a-chip with luminal flow and peristaltic-like motility. *Lab Chip* 18: 3079–3085 (2018).

12. Unger, M. A., Chou, H. P., Thorsen, T., Scherer, A. & Quake, S. R. Monolithic microfabricated valves and pumps by multilayer soft lithography. *Science* 288: 113–116 (2000).

13. Au, A. K., Lai, H., Utela, B. R. & Folch, A. Microvalves and micropumps for BioMEMS. *Micromachines (Basel)* 2: 179 (2011).

14. Bhattacharjee, N., Urrios, A., Kang, S. & Folch, A. The Upcoming 3D-Printing Revolution in Microfluidics. *Lab Chip* 16: 1720 (2016).

15. Zhang, M., Wu, J., Wang, L., Xiao, K. & Wen, W. A simple method for fabricating multi-layer PDMS structures for 3D microfluidic chips. *Lab Chip* 10: 1199–1203 (2010).

16. Bhattacharjee, N., Urrios, A., Kang, S. & Folch, A. The upcoming 3D-printing revolution in microfluidics. *Lab Chip* 16: 1720–1742 (2016).

17. Gong, H., Woolley, A. T. & Nordin, G. P. High density 3D printed microfluidic valves, pumps, and multiplexers. *Lab Chip* 16: 2450–2458 (2016).

18. Au, A. K., Bhattacharjee, N., Horowitz, L. F., Chang, T. C. & Folch, A. 3D-printed microfluidic automation. *Lab Chip* 15: 1934–1941 (2015).

19. Lee, Y. S., Bhattacharjee, N. & Folch, A. 3D-printed Quake-style microvalves and micropumps. *Lab Chip* 18: 1207–1214 (2018).

20. Sochol, R. D. *et al.* 3D printed microfluidic circuitry via multijet-based additive manufacturing. *Lab Chip* 16: 668–678 (2016).

21. Alsharhan, A. T., Stair, A. J., Utz, R. R., Lamont, A. C., Restaino, M. A., Acevedo, R. & Sochol, R. D. A 3D Nanoprinted Normally Closed Microfluidic Transistor. *Proceedings of*

the IEEE International Conference on Micro Electro Mechanical Systems (MEMS) 2020: 131 (2020).

22. Li, S., Chen, X., Li, X., Tian, H., Wang, C., Nie, B., He, J. & Shao, J. Bioinspired robot skin with mechanically gated electron channels for sliding tactile perception. *Sci Adv* 8: eade0720 (2022).

23. Guo, M., Wang, C., Yang, Z., Xu, Z., Yang, M., Zhao, P., Zhou, Y., Li, P., Wang, Q. & Li, Y. Controllable and Scalable Fabrication of Superhydrophobic Hierarchical Structures for Water Energy Harvesting. *Electronics (Basel)* 11: (2022).

24. Chen, X., Luo, Y., Chen, Y., Li, S., Deng, S., Wang, B., Zhang, Q., Li, X., Li, X., Wang, C., He, J., Tian, H. & Shao, J. Biomimetic Contact Behavior Inspired Tactile Sensing Array with Programmable Microdomes Pattern by Scalable and Consistent Fabrication. *Advanced Science* 11: 2408082 (2024).

25. Chen, X., Wang, B., Duan, J., Yang, B., Wang, L., Li, S., Luo, Y., Luo, S., Sun, B., Wang, C., Tian, H., Li, X., Lv, J. & Shao, J. Compression-Durable Soft Electronic Circuits Enabled by Embedding Self-Healing Biphasic Liquid-Solid Metal Into Microstructured Elastomeric Channels. *Advanced Materials* 37: 2420469 (2025).

26. Hevia, E. G., McCann, C. M., Bell, M., Hyun, N. P., Majidi, C., Bertoldi, K. & Wood, R. J. High-Gain Microfluidic Amplifiers: The Bridge between Microfluidic Controllers and Fluidic Soft Actuators. *Advanced Intelligent Systems* 4: 2200122 (2022).

27. Conrad, S., Teichmann, J., Auth, P., Knorr, N., Ulrich, K., Bellin, D., Speck, T. & Tauber, F. J. 3D-printed digital pneumatic logic for the control of soft robotic actuators. *Sci Robot* 9: (2024).

28. Hubbard, J. D., Acevedo, R., Edwards, K. M., Alsharhan, A. T., Wen, Z., Landry, J., Wang, K., Schaffer, S. & Sochol, R. D. Fully 3D-printed soft robots with integrated fluidic circuitry. *Sci Adv* 7: eabe5257 (2021).

29. Zhai, Y., De Boer, A., Yan, J., Shih, B., Faber, M., Speros, J., Gupta, R. & Tolley, M. T. Desktop fabrication of monolithic soft robotic devices with embedded fluidic control circuits. *Sci Robot* 8: eadg3792 (2023).

30. Preston, D. J., Rothemund, P., Jiang, H. J., Nemitz, M. P., Rawson, J., Suo, Z. & Whitesides, G. M. Digital logic for soft devices. *Proc Natl Acad Sci U S A* 116: 7750–7759 (2019).

31. Vo, V. T., Rajappan, A., Jumet, B., Bell, M. D., Urbina, S. & Preston, D. J. Sheet-Based Fluidic Diodes for Embedded Fluidic Circuitry in Soft Devices. *Advanced Intelligent Systems* 6: (2024).

32. Wehner, M., Truby, R. L., Fitzgerald, D. J., Mosadegh, B., Whitesides, G. M., Lewis, J. A. & Wood, R. J. An integrated design and fabrication strategy for entirely soft, autonomous robots. *Nature* 536: 451–455 (2016).

33. Hoang, S., Karydis, K., Brisk, P. & Grover, W. H. A pneumatic random-access memory for controlling soft robots. *PLoS One* 16: e0254524 (2021).

34. Gao, R. Z., Ngoc, V., Mai, T., Levinski, N., Kormylo, J. M., Murdock, R. W., Dickerson, C. R. & Ren, C. L. A novel air microfluidics-enabled soft robotic sleeve: Toward realizing innovative lymphedema treatment. *Biomicrofluidics* 16: 34101 (2022).

35. Gao, R. Z. & Ren, C. L. Synergizing microfluidics with soft robotics: A perspective on miniaturization and future directions. *Biomicrofluidics* 15: 11302 (2021).

36. Filippi, M., Yasa, O., Kamm, R. D., Raman, R. & Katzschmann, R. K. Will microfluidics enable functionally integrated biohybrid robots? *Proc Natl Acad Sci U S A* 119: e2200741119 (2022).

37. Dabbagh, S. R., Sarabi, M. R., Birtek, M. T., Seyfi, S., Sitti, M. & Tasoglu, S. 3D-printed microrobots from design to translation. *Nat Commun* 13: 5875 (2022).

38. Choi, J. W., MacDonald, E. & Wicker, R. Multi-material microstereolithography. *Int. J. Adv. Manuf. Technol.* 49: 543–551 (2010).

39. Han, D., Yang, C., Fang, N. X. & Lee, H. Rapid multi-material 3D printing with projection micro-stereolithography using dynamic fluidic control. *Addit Manuf* 27: 606–615 (2019).

40. Kim, Y. T., Castro, K., Bhattacharjee, N. & Folch, A. Digital manufacturing of selective porous barriers in microchannels using multi-material stereolithography. *Micromachines (Basel)* 9: 125 (2018).

41. Gopinathan, K. A., Mishra, A., Mutlu, B. R., Edd, J. F. & Toner, M. A microfluidic transistor for automatic control of liquids. *Nature* 622: 735–741 (2023).

42. Bhattacharjee, N., Parra-Cabrera, C., Kim, Y. T., Kuo, A. P. & Folch, A. Desktop-Stereolithography 3D-Printing of a Poly(dimethylsiloxane)-Based Material with Sylgard-184 Properties. *Advanced Materials* 30: 1800001 (2018).

43. Fleck, E., Keck, C., Ryszka, K., DeNatale, E. & Potkay, J. Low-Viscosity Polydimethylsiloxane Resin for Facile 3D Printing of Elastomeric Microfluidics. *Micromachines (Basel)* 14: 773 (2023).

44. Kuo, A. P., Bhattacharjee, N., Lee, Y.-S., Castro, K., Kim, Y. T. & Folch, A. High-Precision Stereolithography of Biomicrofluidic Devices. *Adv Mater Technol* 1800395 (2019) doi:10.1002/admt.201800395.

45. Naderi, A., Bhattacharjee, N. & Folch, A. Digital Manufacturing for Microfluidics. *Annu Rev Biomed Eng* 21: 325–364 (2019).

46. Gong, H., Woolley, A. T. & Nordin, G. P. 3D printed high density, reversible, chip-to-chip microfluidic interconnects. *Lab Chip* 18: 639–647 (2018).

47. Nielsen, A. V, Beauchamp, M. J., Nordin, G. P. & Woolley, A. T. 3D Printed Microfluidics. *Annu Rev Anal Chem* 13: 45–65 (2020).

48. Ahmadianyazdi, A., Miller, I. J. & Folch, A. Tunable resins with PDMS-like elastic modulus for stereolithographic 3D-printing of multimaterial microfluidic actuators. *Lab Chip* 23: 4019 (2023).

49. Kim, Y. T., Ahmadianyazdi, A. & Folch, A. A 'print–pause–print' protocol for 3D printing microfluidics using multimaterial stereolithography. *Nat Protoc* 18: 1243 (2023).

50. Sagot, M., Derkenne, T., Giunchi, P., Davit, Y., Nougayrède, J.-P., Tregouet, C., Raimbault, V., Malaquin, L. & Venzac, B. Functionality integration in stereolithography 3D printed microfluidics using a 'print-pause-print' strategy. *Lab Chip* 24: 3508 (2024).

51. Sedra, A. S. & Smith, K. C. *Microelectronic Circuits*. (Oxford University Press, 2010).

52. Liu, X., Song, H., Zuo, W., Ye, G., Jin, S., Wang, L. & Li, S. Theoretical and Experimental Studies of a PDMS Pneumatic Microactuator for Microfluidic Systems. *Energies (Basel)* 15: 1–19 (2022).

53. Wang, R.-Q., Lin, T., Shamshery, P. & Winter, A. G. Control of Flow Limitation in Flexible Tubes. *Journal of Mechanical Design* 139: (2017).

54. Shapiro, A. H. Steady Flow in Collapsible Tubes. *J Biomech Eng* 99: 126–147 (1977).

55. Wilson, T. A., Rodarte, J. A. & Butler, J. P. Wave-speed and viscous flow limitation. in *Handobook of Physiology: The Respiratory System. Vol. 3* (eds. Macklem, P. & Mead, J.) 55–61 (American Physiological Society, 1986).

56. Kamm, R. D. & Pedley, T. J. Flow in collapsible tubes: a brief review. *J. Biomech. Eng.* 111: 177–179 (1989).

57. Matsuzaki, Y., Ikeda, T., Kitagawa, T. & Sakata, S. Analysis of Flow in a Two-Dimensional Collapsible Channel Using Universal “Tube” Law. *J. Biomech. Eng.* 116: 469–476 (1994).

58. Whittaker, R. J., Heil, M., Jensen, O. E. & Waters, S. L. A rational derivation of a tube law from shell theory. *Quarterly journal of mechanics and applied mathematics* 63: 465–496 (2010).

59. Anand, V. & Christov, I. C. Revisiting steady viscous flow of a generalized Newtonian fluid through a slender elastic tube using shell theory. *ZAMM Zeitschrift fur Angewandte Mathematik und Mechanik* 101: e201900309 (2021).

60. Black, H. S. Stabilized Feedback Amplifiers. *Bell Syst. Tech. J.* 13: 1–18 (1934).

61. Horowitz, P. & Hill, W. *The Art of Electronics*. (Cambridge University Press, 2015).

62. Weaver, J. A., Melin, J., Stark, D., Quake, S. R. & Horowitz, M. A. Static control logic for microfluidic devices using pressure-gain valves. *Nat Phys* 6: 218–223 (2010).

63. Toepke, M. W., Abhyankar, V. V. & Beebe, D. J. Microfluidic logic gates and timers. *Lab Chip* 7: 1449 (2007).

64. Grover, W. H., Ivester, R. H. C., Jensen, E. C. & Mathies, R. A. Development and multiplexed control of latching pneumatic valves using microfluidic logical structures. *Lab Chip* 6: 623–631 (2006).

65. Jensen, E. C., Grover, W. H. & Mathies, R. A. Micropneumatic Digital Logic Structures for Integrated Microdevice Computation and Control. *Microelectromechanical Systems, Journal of* 16: 1378–1385 (2007).

66. Duncan, P. N., Nguyen, T. V. & Hui, E. E. Pneumatic oscillator circuits for timing and control of integrated microfluidics. *Proceedings of the National Academy of Sciences* 110: 18104–18109 (2013).

67. Kim, S.-J., Yokokawa, R. & Takayama, S. Microfluidic oscillators with widely tunable periods. *Lab Chip* 13: 1644 (2013).

68. Kim, S. J., Yokokawa, R., Lesher-Perez, S. C. & Takayama, S. Multiple independent autonomous hydraulic oscillators driven by a common gravity head. *Nat Commun* 6: 7301 (2015).

69. Naming the transistor. *PBS.org* https://www.pbs.org/transistor/album1/pierce/naming.html (1999).

70. Kim, S. J., Yokokawa, R. & Takayama, S. Analyzing threshold pressure limitations in microfluidic transistors for self-regulated microfluidic circuits. *Appl Phys Lett* 101: (2012).

71. Wang, Z., Volinsky, A. A. & Gallant, N. D. Crosslinking effect on polydimethylsiloxane elastic modulus measured by custom-built compression instrument. *J. Appl. Polymer Sci.* 131: 41050 (2014).

72. Xiang, H., Wang, X., Ou, Z., Lin, G., Yin, J., Liu, Z., Zhang, L. & Liu, X. UV-curable, 3D printable and biocompatible silicone elastomers. *Prog Org Coat* 137: 105372 (2019).

73. Au, A. K., Lee, W. & Folch, A. Mail-order microfluidics: evaluation of stereolithography for the production of microfluidic devices. *Lab Chip* 14: 1294–1301 (2014).

74. Chen, Z., Lv, Z., Zhang, Z., Hébert, M., Huissoon, J. & Ren, C. L. A quantitative study of the dynamic response of compliant microfluidic chips in a microfluidics context You may also like Biomaterials for microfluidic technology A quantitative study of the dynamic response of compliant microfluidic chips in a microfluid. *J. Micromech. Microeng* 32: 9 (2022).

75. Gervais, T., El-Ali, J., Günther, A. & Jensen, K. F. Flow-induced deformation of shallow microfluidic channels. *Lab Chip* 6: 500–507 (2006).

76. Thrasher, C. J., Schwartz, J. J. & Boydston, A. J. Modular Elastomer Photoresins for Digital Light Processing Additive Manufacturing. *ACS Appl Mater Interfaces* 9: 39708–39716 (2017).

77. Takeoka, Y., Liu, S. & Asai, F. Improvement of mechanical properties of elastic materials by chemical methods. *Sci Technol Adv Mater* 21: 817–832 (2021).

78. Boaks, M., Roper, C., Viglione, M., Hooper, K., Woolley, A. T., Christensen, K. A. & Nordin, G. P. Biocompatible High-Resolution 3D-Printed Microfluidic Devices: Integrated Cell Chemotaxis Demonstration. *Micromachines (Basel)* 14: 1589 (2023).

79. Urrios, A., Parra-Cabrera, C., Bhattacharjee, N., Gonzalez-Suarez, A. M., Rigat-Brugarolas, L. G., Nallapatti, U., Samitier, J., DeForest, C. A., Posas, F., Garcia-Cordero,

J. L. & Folch, A. 3D-printing of transparent bio-microfluidic devices in PEG-DA. *Lab Chip* 16: 2287–2294 (2016).

80. Musgrove, H. B., Cook, S. R. & Pompano, R. R. Parylene-C Coating Protects Resin-3D-Printed Devices from Material Erosion and Prevents Cytotoxicity toward Primary Cells. *ACS Appl Bio Mater* 6: 3079–3083 (2023).

81. Lam, E. W., Cooksey, G. A., Finlayson, B. A. & Folch, A. Microfluidic Circuits with Tunable Flow Resistances. *Appl Phys Lett* 89: 164105 (2006).

82. Sarpeshkar, R. Analog Versus Digital: Extrapolating from Electronics to Neurobiology. *Neural Comput* 10: 1601–1638 (1998).

83. Sauro, H. M. & Kim, K. It's an analog world. *Nature* 497: 572–573 (2013).

84. Sanchez Noriega, J. L., Chartrand, N. A., Valdoz, J. C., Cribbs, C. G., Jacobs, D. A., Poulson, D., Viglione, M. S., Woolley, A. T., Van Ry, P. M., Christensen, K. A. & Nordin, G. P. Spatially and optically tailored 3D printing for highly miniaturized and integrated microfluidics. *Nat Commun* 12: 5509 (2021).

85. Rogers, C. I., Qaderi, K., Woolley, A. T. & Nordin, G. P. 3D printed microfluidic devices with integrated valves. *Biomicrofluidics* 9: 16501 (2015).

86. Duncan, P. N., Ahrar, S. & Hui, E. E. Scaling of pneumatic digital logic circuits. *Lab Chip* 15: 1360–1365 (2015).

87. Byvaltsev, V. A., Bardonova, L. A., Onaka, N. R., Polkin, R. A., Ochkal, S. V, Shepelev, V. V, Aliyev, M. A. & Potapov, A. A. Acridine Orange: A Review of Novel Applications for Surgical Cancer Imaging and Therapy. *Front Oncol* 9: 925 (2019).